Fabrication of hybrid thin film based on bacterial cellulose nanocrystals and metal nanoparticles with hydrogen sulfide gas sensor ability

Pongpat Sukhavattanakul[a,b], Hathaikarn Manuspiya[a,b,*]

[a] The Petroleum and Petrochemical College, Chulalongkorn University, Soi Chula 12, Phyathai Road, Pathumwan, Bangkok, 10330, Thailand
[b] Center of Excellence on Petrochemicals and Materials Technology, Chulalongkorn University, Bangkok, 10330, Thailand

ABSTRACT

The nanocrystalline structures of bacterial cellulose (BC) are described as "environmentally friendly green nanomaterials". Bacterial cellulose (BC) was produced from *Gluconacetobacter xylinus* in pellicle form with a large bundle of fibers were acid hydrolyzed to obtain bacterial cellulose nanocrystals (BCNCs). The H_2SO_4 acid-hydrolyzed BCNCs were evaluated for their smallest crystallite size and hydrodynamic size, highly negative ζ-potential value, and the highest specific surface area to interact with metallic nanoparticles. Hybrid thin film of BCNCs based surface-loaded silver nanoparticles (AgNPs) and alginate-molybdenum trioxide nanoparticles (MoO_3NPs) was developed for hydrogen sulfide (H_2S) gas sensor. Sensor characteristics were investigated as well as its response with H_2S gas. The film was successfully detected H_2S gas. The color of the film changed by the shift of oxidation number of MoO_3NPs. Once activated by AgNPs, MoO_3NPs was readily reduced to a colored sub-oxide by atomic hydrogen that produced and received from reaction of H_2S gas.

1. Introduction

Almost ten years of advances in natural-based or bio-based polymer research have proved the potential and importance of biopolymers for a wide variety of applications, specifically for biopolymers formed by microorganisms or microbs, including bacterial cellulose nanocrystals (BCNCs) (Jozala et al., 2016; Lin, Huang, & Dufresne, 2012; Ummartyotin & Manuspiya, 2015). Apart from plant-derived cellulose, certain microbial-derived cellulose or bacterial cellulose produced by *Gluconacetobacter xylinus*, tunicate, and algae are also known to produce cellulose in considerable quantities in a relatively pure form even though the chemical structure is similar (George, Ramana, Bawa, & Siddaramaiah, 2011; Shah, Islam, Khattak, & Park, 2013). Bacterial cellulose (BC) has unique properties because of its high purity (no hemicellulose or lignin), higher surface area as compared to native cellulose, high crystallinity, high water swelling, moldability, good shape retention, excellent mechanical and thermal properties (Ashjaran, Yazdanshenas, Rashidi, Khajavi, & Rezaee, 2013; Corrêa, de Morais Teixeira, Pessan, & Mattoso, 2010; Fu, Zhang, & Yang, 2013; George et al., 2011; Jozala et al., 2016; Lin & Dufresne, 2014; Shah et al., 2013; Singhsa, Narain, & Manuspiya, 2018; Tang, Sisler, Grishkewich, & Tam, 2017; Vasconcelos et al., 2017).

In the area of nanomaterials technology, the top-down approaches

(e.g.: homogenization, hydrolysis, combined chemical-mechanical processes) can be applied to downsize the plant-derived cellulose or microbial-derived fibers in small particles as cellulose nanocrystals (CNCs) suspensions, expanding versatility and new nanomaterials resources to this cellulosic material (Lin et al., 2012; Vasconcelos et al., 2017). These CNCs have unique nano-porous three-dimensional network at nanometric scales (Fu et al., 2013), and they dominates various attractive characteristics, such as large surface area, easy surface modification, and high aspect ratios which can facilitate the penetration of inorganic nanoparticles or metallic ions into the CNCs structure.

Acid hydrolysis, especially in the strong inorganic acids, such as H_2SO_4 and HCl are the most commonly used method for producing CNCs (Dufresne, 2012) by penetrating of hydrogen ions (H^+) into amorphous cellulose molecules promoting cleavage of covalent or glycosidic linkage/bonds, therefore releasing single crystallites (Vasconcelos et al., 2017). H_2SO_4 produces a highly stable colloidal suspension because of the high negative surface charge contributed by sulfonation of the CNCs surface. However, the presence of sulfate groups ($-OSO_3-$) reduces the thermal stability of the nanocrystals (Martínez-Sanz, Lopez-Rubio, & Lagaron, 2011). In contrast, when HCl is used, a low-density surface charges is produced on the CNCs with limited nanocrystal dispersibility, which tends to contribute sediment in aqueous suspensions. Some studies describe the companion use of

H_2SO_4 and HCl to generate stable and thermally resistant CNCs suspensions (Corrêa et al., 2010). CNCs with different physical and mechanical properties can be yielded by the acid hydrolysis reaction conditions, which depend on the concentration and type of acid, reaction time, and temperature. Many types of BCNCs have been developed for numerous applications, including textile industry, nonwoven cloth, paper, food, waste treatment, broadcasting, mining, refineries (Ashjaran et al., 2013; Lin & Dufresne, 2014; Wu & Liu, 2012), drug delivery systems, vascular grafts, and scaffolds for tissue engineering in vitro and in vivo (Jozala et al., 2016).

Hydrogen sulfide (H_2S) gas is a colorless, flammable, extremely hazardous gas with the characteristic of a "rotten egg" smell (Chen, Wang, Hartman, & Zhou, 2008; Schirmer, Heir, & Langsrud, 2009). It often results from the microbial breakdown of organic materials in the absence of oxygen. Since, it is a chemical suffocate, which could cause to lose consciousness even at a very low concentration, paralyze the lungs and affects human's nervous system (Choudhary, Singh, Mishra, & Dwivedi, 2013; Gahlaut, Yadav, Sharan, & Singh, 2017; Malone Rubright, Pearce, & Peterson, 2017; Pandey, Kim, & Tang, 2012), and at a very high concentration (> 700 ppm) it could cause death by reducing the oxygen-carrying capacity of the blood, by interrupting the oxidative processes of tissue cells, and by paralyzing the nervous system leading to respiratory failure (Chen, Morris, & Whitmore, 2013; Gahlaut et al., 2017). According to the potential hazardous nature of H_2S gas, it is important to detect for both human health and industrial control purposes, especially in the terms of raw meat products of food packaging industry (Sarfraz et al., 2014). Moreover, H_2S gas is one of the most often encountered food spoilage gases in meat packaging systems, which is generated by the reason of microbial spoilage and lipid oxidation (Murphy, O'Grady, & Kerry, 2013) can change the headspace gas composition in the package headspace (Coombs, Holman, Friend, & Hopkins, 2017; Mohebi & Marquez, 2015). Accordingly, many smart packaging technologies based on sensor label have been explored during recent decades. The sensor label could be in the form of smart labels, immobilized, or printed on/inside the packaging films, which would enable to detect the level of gaseous or volatile organic compound (VOC) content increases during the spoilage either by bacteria or enzymic degradation (Brockgreitens & Abbas, 2016; Coombs et al., 2017; McMillin, 2017; Remenant, Jaffrès, Dousset, Pilet, & Zagorec, 2015; Sofos, 1994) and caution about the quality and safety of the meat products by changing in their color or visible spot.

Recently, the use of hybrid material, which are consisted of two constituents at nanometric scale. Commonly, in the organic–inorganic matrices, these materials revealed a significant improvement in mechanical properties of nanocomposites consisting of nanoparticles dispersed within the matrix phase for expanding the application range of these materials (Gonçalves et al., 2013). For the use of inorganic materials in association with almost any hybrid materials were reported and developed for volatile substances and gasses sensor. Some recently reported the integration of cellulosic materials with metal oxides with the aim of preparing a hybrid or composite allowing high accessibility to more or less aggregated nanoparticles of incorporation with the oxide (Shimizu, Imai, Hirashima, & Tsukuma, 1999). Moreover, bacterial cellulose, has been revealed to be a potential to offer isotropic 3D nano-scaffold for perfect being host these inorganic compounds at the nano-scale, resulting in improvement of the inorganic phase activity, ascribed to the use of BC with high specific surface area (Foresti, Vázquez, & Boury, 2017). For example, the simplest way to achieve the integrated BC and metal-oxide nanoparticles is to mix them under vigorous stirring (Zhang et al., 2016). Besides, a number of semiconductors, such as MoO_3 (Kabcum et al., 2016; Li et al., 2017; MalekAlaie, Jahangiri, Rashidi, HaghighiAsl, & Izadi, 2015), SnO_2 (Kabcum et al., 2016; Sarala Devi, Manorama, & Rao, 1995), α-Fe_2O_3 (Kersen & Holappa, 2006), ZnO (Wang, Chu, & Wu, 2006), In_2O_3 (Xu, Wang, & Shen, 2006), WO_3 (Lin, Hsu, Yang, Lee, & Yang, 1994; Solis, Saukko, Kish, Granqvist, & Lantto, 2001), and CuO (Chen et al., 2008)

have been investigated to detect and to monitor trace concentrations of H_2S. Among all reported sensor-based semiconducting metal-oxide, MoO_3 based gas sensors are most widely investigated because of its small size, high sensitivity, fast response, simple construction, and low cost, which has plenty of Lewis-acid sites, exhibits a high reactivity to H_2S, probably because of its high chemical affinity to H_2S (Kabcum et al., 2016; Li et al., 2017; MalekAlaie et al., 2015). However, a very fast and sensitive initial response of silver nanoparticles (AgNPs) and H_2S gas was very interested and reported to be a first-order reaction in AgNPs, and the initial reaction rate was proportional to the gas concentration down to the 1 ppm volume (ppmv) level (Chen et al., 2013). Hence, the suggestion of the H_2S detection using two different classes gas sensor, AgNPs fast reacted directly with H_2S to generate atomic hydrogen and MoO_3NPs will be reduced to a colored sub-oxide by atomic hydrogen, which will become especially interesting in the improvement of hybrid material for H_2S gas sensor.

The aim of this work was to present the design of bacterial cellulose nanocrystals and metal nanoparticles based polysaccharide sodium alginate matrix as a hybrid thin film for H_2S gas sensor. The effect of acid hydrolysis on bacterial cellulose nanocrystals preparation was investigated. Preliminary experiments with H_2S gas exposure at room temperature with time-varying have been performed. The different concentrations of H_2S gas, especially at higher concentration, of course, reduce more Mo oxidation state, but this is out of the scope of this manuscript.

2. Materials and methods

2.1. Materials

K. xylinus strain (TISTR No. 975) was purchased from the Microbiological Resource Center, Thailand Institute of Scientific and Technological Research (TISTR) (http://www.tistr.or.th/mircen/index.html). D-glucose anhydrous, yeast extract, peptone, and calcium carbonate ($CaCO_3$), sulfuric acid (H_2SO_4), hydrochloric acid (HCl; ACS reagent, 37 %), Molybdenum (VI) oxide nanopowder (MoO_3NPs), sodium borohydride ($NaBH_4$), sodium alginate, sodium hydroxide (NaOH), and zinc chloride ($ZnCl_2$) were obtained from Sigma-Aldrich. Silver nitrate ($AgNO_3$) was obtained from Merck Chemicals. Sodium sulfide nonahydrate ($Na_2S \cdot 9H_2O$, > 95 %) was purchased from Ajax Fine Chem, Co, LTD, Thailand. Ultrapure water from a Milli-Q water was used for all of the experiments. All chemicals were used as received.

2.2. Production of bacterial cellulose (BC)

The BC hydrogel-like pellicle, biosynthesized by *K. xylinus* strains, was prepared by the partially modified method of (Janpetch, Saito, & Rujiravanit, 2016; Maneerung, Tokura, & Rujiravanit, 2008; Singhsa et al., 2018a). *K. xylinus* strains was cultured on agar containing 100 g of D-glucose anhydrous, 10 g of yeast extract, 5 g of peptone, 20 g of $CaCO_3$, and 25 g/L of agar at a temperature of 30 °C for 3 days. A sterilized 100 mL glucose yeast extract nutrient broth (GYNB) solution consisted of D-glucose anhydrous 5.0.% (w/v) and yeast extract 1.0.% (w/v) in Milli-Q ultrapure water was prepared to suspend two ampoules of the freeze-dried cells of *K. xylinus* (TISTR No. 975). The cell suspension was incubated at a temperature of 30 °C for 24 h. The 50 mL of bacteria inoculum was introduced into 2 L of GYNB and incubated at 30 °C for 7 days under static conditions. After incubation, the BC pellicle was produced on the surface of culture GYNB and then rinsed with distilled water to remove any residual GYNB. The acquired BC pellicle was purified by boiling in 2 % (w/v) NaOH solution at a temperature of 80 °C for 1 h and then rinsed repeatedly several times with deionized (DI) water to gain the purified neutral BC pellicle.

2.3. Preparation of bacterial cellulose nanocrystals (BCNCs)

The purified BC pellicles were mechanically disintegrated to a BC paste using a laboratory blender at $5000 - 6000$ rpm for about 15 min under ambient temperature. The BC paste was filtered through filter paper (Whatman No. 1) to remove excess water prior to acid hydrolysis. BCNCs were prepared through acid hydrolysis. The BC paste was hydrolyzed with acid solution in a ratio of 1:20 g/mL with continuous stirring in different conditions as follows: the 65 % H_2SO_4 acid solution with time-varying for 1, 2, and 3 h at 45 °C for H_2SO_4 hydrolysis by the partially modified method of (George et al., 2011) and the 4 N HCl solution with time-varying for 4, 5, and 6 h at reflux temperature for HCl hydrolysis (designated as BCNCs-1 to BCNCs-6) (see Table S1).

The hydrolyzed BCNCs suspension from each acid hydrolysis reactions were then added an excess of DI water (5-fold) and cooled with an ice bath to terminate acid hydrolysis reaction. The excess acidic solution was removed by centrifugation at 10,000 rpm at 4 °C for 10 min for precipitating the BCNCs and then poured out the excess acidic solution. The precipitated BCNCs was collected and dialyzed (MWCO > 12,000) against DI water to gain the neutral BCNCs. After that, the neutral BCNCs was collected by centrifugation at 10,000 rpm at 4 °C for 10 min. Finally, the BCNCs was removed an excess water by freeze-drying at -55 °C for 24 h to collect the dried-BCNCs.

2.4. Preparation of BCNCs based surface-loaded AgNPs (BCNCs–AgNPs)

Freeze-dried BCNCs surface were pre-loaded with silver ion (Ag^+) by immersing in 1 mM of the aqueous $AgNO_3$ under ultrasonic treatment by using a high intensity ultrasonic bath (GT SONIC-D3) at frequency of 40 kHz for 3 h. After an ultrasonic treatment in $AgNO_3$, BCNCs–Ag^+ were then rinsed with ethanol for ca. 30 s to eliminate the Ag^+ that were unadhered and loosely adhered to the BCNCs surface. After that, the Ag^+ saturated–BCNCs were ion-reduced in 100 mM of the aqueous $NaBH_4$ ($NaBH_4$:$AgNO_3$ molar ratio of 100:1) for 20 min and rinsed several times (5 min each) with ultra-pure water to eliminate all traces of chemicals, by the partially modified method of (Maneerung et al., 2008). Finally, the obtained samples were frozen at -40 °C and freeze-dried at -55 °C for 24 h to get BCNCs–AgNPs samples.

2.5. Preparation of alginate-MoO₃NPs solution

A 4 wt% homogeneous sodium alginate solution was prepared by dissolving sodium alginate powder in ultra-pure water at 60 °C for 4 h under magnetic stirrer at a stirring speed of 1000 rpm. In parallel, MoO_3NPs solution was prepared by dissolving required amount of 100 mM in ultra-pure water at room temperature for 2 h under ultrasonic treatment by using a high intensity ultrasonic bath (GT SONIC-D3) at frequency of 40 kHz. Half the volume of the 4 wt% homogeneous sodium alginate and 100 mM MoO_3NPs solution were mixed at room temperature for 2 h under magnetic stirrer at a stirring speed of 800 rpm to reach a final concentration of 2 wt% alginate–50 mM MoO_3NPs solution.

## 2.6. Preparation of hybrid BCNCs–AgNPs and alginate–MoO₃NPs film

The hybrid BCNCs based surface-loaded AgNPs and alginate–MoO_3NPs film was prepared by immersing 0.1 dry wt% of the freeze-dried BCNCs-AgNPs in the 2 wt% alginate-50 mM MoO_3NPs solution at room temperature for 1 h under magnetic stirrer at a stirring speed of 800 rpm. After then, the homogeneous BCNCs–AgNPs/alginate–MoO_3NPs solution was appeared with a very light-grey color, was poured in a round-shaped poly(tetrafluoroethylene) (PTFE) or teflon mold (10 mm height; 4 mm depth; 20 mm diameter), then allowed to air-dry at ambient temperature for 48 h to obtain the BCNCs–AgNPs/alginate–MoO_3NPs film samples (20 mm diameter; thickness 90 μm) and stored under dry conditions.

2.7. Preparation of H₂S gas samples and gas exposure experiment

The ZnS powder was prepared by a simple and efficient one-pot synthesis of sodium sulfide nonahydrate ($Na_2S \cdot 9H_2O$) and zinc chloride ($ZnCl_2$), by the partially modified method of (Infahsaeng & Ummartyotin, 2017), as follow: 1 moL of $ZnCl_2 \cdot 7H_2O$ was prepared in 500 mL of DI water under magnetic stirrer at a stirring speed of 600 rpm for 30 min at temperature of 60 °C. In parallel, 1 mol of $Na_2S \cdot 9H_2O$ was prepared in 500 mL of DI water under magnetic stirrer at a stirring speed of 600 rpm for 30 min at 60 °C, and then added to 1 mol of $ZnCl_2$ solution under magnetic stirrer at a stirring speed of 600 rpm for 1 h at 60 °C. The stoichiometric of chemical reaction is

$$Na_2S \bullet 9H_2O \ (aq) + ZnCl_2 \bullet 7H_2O \ (aq) \rightarrow ZnS \ (s) \ + Na^+ + Cl^-$$

After then, the aqueous suspension of ZnS was rinsed for 10 min with methanol to eliminate all traces of chemicals, centrifuged at 10,000 rpm for 20 min at 4 °C to obtain the sediment ZnS, and then kept in oven at 100 °C for 24 h to obtain the ZnS powder. H_2S gas was prepared at ambient temperature (25 °C) by the reaction of 50 mM ZnS powder with an aqueous solution of 100 mM HCl (in molar ratio 1:2) in a 500 mL tightly septum-capped glass bottle, which was flushed with nitrogen gas and stored at room temperature for 1 h. The excess HCl solution could prevent diffusion of generated H_2S into the reaction solution (Carpenter, Rosolina, & Xue, 2017). The stoichiometric of chemical reaction is

$$ZnS \ (s) \ + 2HCl \ (aq) \rightarrow H_2S \ (s) + ZnCl_2 \ (aq)$$
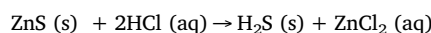
The prepared H_2S gas was calculated the mass and conversed in a concentration of ppm by following Eqs. (1)–(3):

$$PV = Nk_BT \tag{1}$$

$$n = N/N_A \tag{2}$$

$$m = nM_A \tag{3}$$

Where P is the standard ambient pressure (1.01325×10^5 Pa), V is the volume of gas container (5×10^{-4} M^3), N is the gas molecules, k_B is the Boltzmann's constant (1.38×10^{-23} J K^{-1}), T is the standard ambient temperature (298.15 K for 25 °C), n is a number of H_2S moles, N_A is Avogadro's number (6.023×10^{23}), M_A is the molecular weight of H_2S gas (34.08 g mol^{-1}), m is the mass of H_2S gas. Standard temperature and pressure (STP) is defined as a condition of 100.00 kPa (1 bar) and 273.15 K (0 °C), which is a standard of the International Union of Pure and Applied Chemistry (IUPAC). Thus, the concentration of H_2S gas was calculated to be approximately 1400 ppm in the 500 mL tightly septum-capped glass bottle. The H_2S gas was diluted 100 times by displaced 5 mL of the H_2S gas using syringe plunger to each of the film sample bottles with the same bottle volume. Finally, each of the film sample bottles was contained the H_2S gas in concentration of approximately 14 ppm. For the H_2S gas exposure of BCNCs–AgNPs/alginate–MoO_3NPs film samples. Prior to gas exposure, the film samples were prepared for different gas exposure time (5 min, 1 h, and 24 h) by placing in different of the 500 mL septum-capped glass bottle with an identifying mark. The film samples in the septum-capped glass bottle with an identifying mark were subsequently exposed to the H_2S gas, as follow: insert a clean needle of the syringe into the septum at the top of the bottle cap, the gas pressure in the bottle was displaced into the syringe plunger, waited for the gas volume to reach 5 mL, and then transferred the gas to each of the film sample bottles.

2.8. Characterization

BC production was reported as the dry weight of cellulosic fibers within the volume of bacterial culture media in liter (g/L). The dry weight of BC pellicle was obtained by freezing at -40 °C for 24 h prior to freeze-drying technique at -55 °C for 24 h. The chemical structures of

all samples were investigated by using an attenuated total reflectance fourier transform infrared (ATR-FTIR, Nicolet Nexus 670 FT-IR spectrometer). All spectra were scanned between 4000 and 650 cm^{-1} at a resolution of 32 cm^{-1}. OPUS 5.5 software (Bruker Optics GmbH, Ettlingen, Germany) was used for IR spectral acquisition. The I$_\alpha$ fraction of the bacterial cellulose samples were calculated by the following equations obtained from (Bi et al., 2014; Singhsa et al., 2018a; Singhsa, Narain, & Manuspiya, 2018), equation parameters proposed by Yamamoto, Horii, and Hirai (1996).:

$$f_\alpha = 2.55 \, f_{\alpha IR} - 0.32 \tag{4}$$

where f$_{\alpha IR}$ can be calculated as $A_\alpha /(A_\alpha + A_\beta)$ and A_α and A_β are the integrated intensities from the absorbencies at corresponding wavenumber 750 and 710 cm^{-1}, respectively.

XRD diagrams of dried pristine BC and dried BCNCs samples were recorded using a Rigaku model SmartLab 4800 diffractometer with a Cu Kα radiation wavelength (λ = 1.54 Å), generated at a voltage of 40 kV and a filament emission of 30 mA. Samples were scanned from the 2θ = 5 to 80° range at a scan speed of 2°/min and a scan step of 0.02°. The average crystallite size (L$_{hkl}$) were calculated based on XRD measurements. L$_{hkl}$ was calculated from the following the Scherrer equation (Eq. (5)):

$$L_{hkl} = K\lambda/\beta_{hkl}cos\theta_{hkl} \tag{5}$$

Where β$_{hkl}$ is the breadth of the peak of a specific phase (*hkl*) or is the full width at half maximum height (FWHM) for the diffraction angle 2θ in radian, K is a constant that varies with the method of taking the breadth (K = 0.94), λ is the wavelength of incident X-rays (1.54 Å), θ is the center angle of the peak (Bragg's angle). The crystallinity (%) was calculated from the following Eq. (6):

$$Cr(\%) = (Sc/St) \times 100 \tag{6}$$

Where S$_c$ is sum of net area and S$_t$ is sum of total area.

The ζ potentials of all acid hydrolyzed-BC suspensions were characterized at 25 °C by Malvern Zetasizer Nano ZSP (Malvern Instruments Ltd., GB).

The Z-discriminant function (Z-value) was calculated using the following Eq. (7) proposed by Wada, Okano, and Sugiyama (2001):

$$Z = 1693d_1 - 902d_2 - 549 \tag{7}$$

where d_1 is the d-spacing of the peaks at 2θ near 15° (I$_\alpha$ (100) and I$_\beta$ (110)) and d_2 is the d-spacing of the peaks at 2θ near 17° (I$_\alpha$ (010) and I$_\beta$ (1–10)). The relative content of cellulose I$_\alpha$/cellulose I$_\beta$ ratio was calculated using the following Eq. (8) proposed by Wada, Kondo, and Okano (2003):

$$f_{\beta X-ray} = -70.542d_1 + 37.583d_2 + 23.360 \tag{8}$$

The hydrodynamic sizes of all acid hydrolyzed-BC suspensions were introduced into the viewing chamber using the integrated fluidics capability by NanoSight NS500 (Malvern Instruments Ltd., GB) by the DLS technique. The reported value is an average of 3 measurements. The total specific surface areas and micro-pore volume of selected samples were characterized by N$_2$ adsorption at the temperature of liquid nitrogen applying the Brunauer-Emmett-Teller (BET) technique (Brunauer, Emmett, & Teller, 1938)) (BELSORP, mini-II nitrogen adsorptometer, Osaka, Japan). As a primary step the samples were subjected to a freeze-drying process, and then evacuated under ambient conditions for 24 h.

The surface morphology of the samples were characterized by field emission scanning electron microscopy (FE-SEM, Hitachi S-4800 model). The freeze-dried pristine BC, freeze-dried BCNCs, and freeze-dried BCNCs–AgNPs were sputter-coated with platinum in preparation for FE-SEM imaging. A Hitachi model S-4800 FE-SEM microscope was used operating at an accelerated voltage of 5 kV and a magnification of 20 × . SEM/EDX was used for the determination of elemental

composition of the freeze-dried BCNCs–AgNPs and the hybrid BCNCs–AgNPs/alginate–MoO$_3$NPs film. Transmission electron microscopy (TEM) micrographs of the pristine BC, BCNCs, and BCNCs–AgNPs samples were taken in a JEOL 100CX-2 transmission electron microscope at an accelerating voltage of 100 kV. Samples were diluted and prepared by dropping the sample suspension on a carbon-coated grid and allowed to dry, followed by staining with a 2 wt % aqueous uranyl acetate solution. Chemical compositions, oxidation state number of MoO$_3$NPs on the hybrid BCNCs–AgNPs/alginate–MoO$_3$NPs film were characterized by x-ray photoelectron spectroscopy (XPS, Kratos Axis Ultra DLD) and with a monochromatic Al Kα as an X-ray source (anode HT = 15 kV) and energy dispersive X-ray analysis (EDX, JSM-7610 F, JEOL). The depth of penetration of XPS is 10 nm.

The binding energies were referenced to the hydrocarbon C 1s peak at 284.6 eV (Susi, Pichler, & Ayala, 2015). Data evaluation was performed using CasaXPS. For fitting of the Mo 5d states, we employed the following parameters (Borgschulte et al., 2017; Ji et al., 2013):

Mo^{4+} : $E_B(5/2) = 229.8$ eV; $E_B(3/2) = 233.1$ eV

Mo^{5+} : $E_B(5/2) = 231.1$ eV; $E_B(3/2) = 234.3$ eV

Mo^{6+} : $E_B(5/2) = 232.8$ eV; $E_B(3/2) = 235.9$ eV

The thickness of each film sample was measured with a digital vernier caliper (Keiba, Japan). Measurements were taken at four different places on the film and an average value were calculated.

3. Results and discussion

3.1. Production of BC, preparation of BCNCs and their properties

For BC production. *K. xylinus* (or *G. xylinus*) strains is the original microbial producer of BCNCs and has become more interesting in the model system for the study and research of biosynthetic mechanisms of BNC in bacteria (Keshk, 2014), because it produces a nearly nanofibrilar film with a gelatinous layer on the opposite side and a denser diagonal surface (Cai & Kim, 2010; Kurosumi, Sasaki, Yamashita, & Nakamura, 2009). For this study, *K. xylinus* strain (TISTR No. 975) was cultured on agar, introduced into 2 L of glucose yeast extract nutrient broth (GYNB), and incubated at 30 °C for 7 days under static conditions. The average yield of freeze-dried BC produced by fermenting with D-glucose as carbon source was 2.25 g/L of culture. The physical appearance of BC pellicle is white-transparent single layer with dense and smooth surface (Fig. 1a–b) and is thus described by a highly crystalline linear polymer of glucose synthesized, absent of hemicellulose, pectin, lignin, or any other compound found in the plant-derived cellulose (Fu et al., 2013).

BCNCs are the crystalline domains hydrolyzed through acid hydrolysis, this method starts with the random cleavage of amorphous phases of very long cellulose micro- fibrils eventually giving raise to several fractions of BC hydrolysis products (George et al., 2011). They are quite rigid, several rod-like particles with an average length of up to hundreds of nanometers (Tang et al., 2017) and width of several nanometers (10 − 50 nm). For preparation of BCNCs, HCl and H$_2$SO$_4$ were
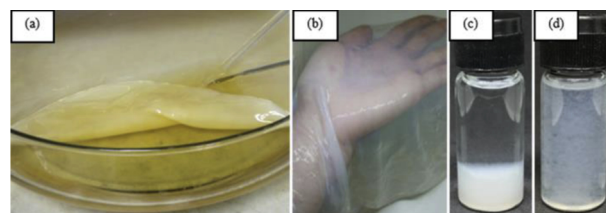

Fig. 1. BC pellicle is formed on the surface of media (GYNB) after incubated at 30 °C for 7 days under static conditions (a), purified neutral BC pellicle (b), Suspension of BCNCs-3 (c) and BCNCs-6 (d).
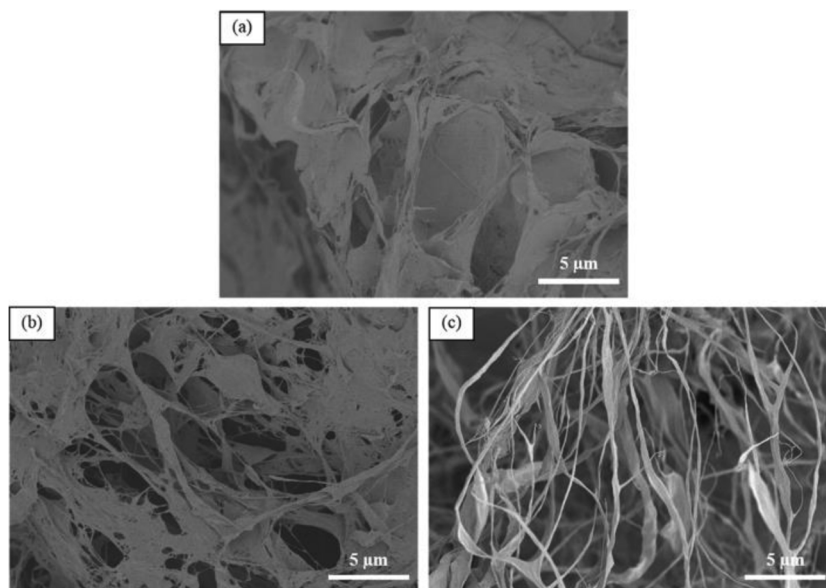
Fig. 2. SEM micrographs of: non-hydrolyzed BC (a), BCNCs-3 (b), and BCNCs-6 (c).

used to obtain BCNCs. Six acid hydrolysis conditions with time-varying were used to evaluate the influence of the acid types and reaction time on BCNCs preparation. H_2SO_4 produces a highly stable colloidal suspension (Fig. 1d) because of the high negative surface charge contributed by sulfonation of the CNCs surface. In contrast, when HCl is used (Fig. 1c) low-density surface charges is produced on the CNCs with limited nanocrystal dispersibility, which tends to contribute sediment in aqueous suspensions.

Some studies describe the companion use of H_2SO_4 and HCl to generate stable and thermally resistant CNCs suspensions (Corrêa et al., 2010). CNCs with different physical and mechanical properties can be yielded by the acid hydrolysis reaction conditions, which depend on the concentration and type of acid, reaction time, and temperature. The abundant thick bundles of BC fibers, which corresponded to the FE-SEM images and the TEM images (Figs. 2a and 3 a). In contrast with HCl-hydrolyzed BC for 6 h (Figs. 2b and 3 b) and H_2SO_4-hydrolyzed BC for 3 h (Figs. 2c and 3 c) that show an increase of single fibers. The integrated structure of BC fiber bundles was broken into separated fibers and many small fiber bundles by penetrating of hydrogen ions (H^+) into amorphous cellulose molecules promoting cleavage of covalent or glycosidic linkage/bonds, therefore releasing single crystallites (Vasconcelos et al., 2017).

3.1.1. Z-discriminant function, I_α/I_β ratio, crystallinity, and crystallite size

The XRD patterns of pristine BC and all acid-hydrolyzed BCNCs showed three 2θ diffraction peaks at around 15°, 17°, and 22° for cellulose I polymorphs (both I_α and I_β allomorphs), which are normally ascribed to crystallographic planes of 110, 010, 100 for Iα and 200, 100, 1–10 for Iβ, respectively (Wada et al., 2001). To analyze and classify all cellulose samples that were the algal-bacterial type (I_α-rich, $Z > 0$) or the cotton-ramie type (I_β-dominant, $Z < 0$) (Wada et al., 2001), the Z-values (Table 1) were calculated by substituting the d_1 and d_2 values listed in Table S2 into the Eq. (7) and plotted in Fig. S1. The intensity of the d_1 is higher than the d_2, which is a distinctive characteristic of typical cellulose that dominate mostly I_α phase (Lee, Gu, Kafle, Catchmark, & Kim, 2015). All samples were small differences in d-spacing by the acid hydrolysis and classified as I_α-rich type (Z-value > 0). Otherwise, the relative content of I_α/I_β were calculated in Table S2. Comparing the I_α/I_β ratios of pristine BC (0.87/0.13), BCNCs-3 (0.83/0.17), and BCNCs-6 (0.9/0.1), the highest of I_α/I_β ratio was found in H_2SO_4-hydrolyzed BCNCs (BCNCs-6) and the lowest of I_α/I_β ratio was found in HCl-hydrolyzed BCNCs (BCNCs-3). The differences notwithstanding, it was observed that the choice of acid hydrolysis conditions slightly affect the I_α/I_β ratio of bacterial cellulose. Nevertheless, the effect is not significant. Crystallinity is a main factor that significantly influences the physical, structural and mechanical properties of materials. Therefore, the XRD patterns obtained from HCl-hydrolyzed BC samples with hydrolysis time-varying at 4, 5, and 6 h (BCNCs-1 to 3) (Fig. 4a), XRD patterns obtained from H_2SO_4-hydrolyzed BC samples with hydrolysis time-varying at 1, 2, and 3 h (BCNCs-4 to 6) (Fig. 4b), and XRD patterns obtained from pristine BC, BCNCs-3 and BCNCs-6 (Fig. 4c) were used to determine the percent crystallinity (Cr (%)) and the crystallite size (L_{hkl}) of pristine BC and all acid-hydrolyzed BCNCs. The results indicated that all BCNCs had a Cr (%) (85.4–90.2.%) greater than pristine BC (81.1.%) (Table 1). The higher in crystallinity after acid hydrolysis reaction was because of a rapid and continuous decrease of the amorphous content, as this amorphous phase is to a higher degree accessible to acid penetration. Crystallinity
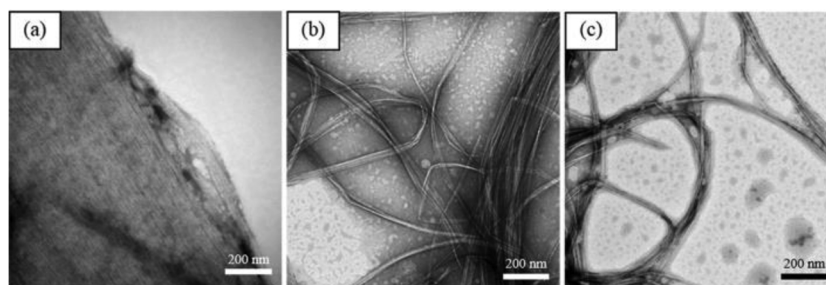

Fig. 3. TEM micrographs of: non-hydrolyzed BC (a), BCNCs-3 (b), and BCNCs- 6 (c). Scale markers correspond to 200 nm.

Table 1
The physicochemical characterization of pristine BC and BCNCs obtained through acid hydrolysis under different conditions.

| Sample	XRD			FT-IR	Zetasizer	BET		Nanosizer
	Crystal size (nm)	Crystallinity (%)	Z-values	Cellulose I_α content (%)	ζ-potential (mV)	Specific surface area, A_s (m²/g)	Micro-pore volume, V_m (cm³(STP)/g)	Hydrodynamic size (d.nm)
Pristine BC	6.9	81.1	+8.47	90.1	n.d.	3.1	0.72	n.d.
BCNCs-1	5.9	86.4	+8.63	91.0	−21.5 ± 4.7	n.d.	n.d.	1153 ± 478.5
BCNCs-2	5.8	88.7	+7.49	91.3	−21.9 ± 4.9	n.d.	n.d.	1142 ± 444.1
BCNCs-3	5.3	90.2	+7.45	91.1	−22.6 ± 4.3	6.0	1.38	1122 ± 338.7
BCNCs-4	4.9	85.4	+8.59	91.8	−33.5 ± 6.6	n.d.	n.d.	868.5 ± 424.4
BCNCs-5	4.7	86.7	+8.99	91.0	−34.2 ± 5.3	n.d.	n.d.	861.8 ± 356.6
BCNCs-6	4.6	88.5	+9.17	92.3	−34.3 ± 6.4	6.3	1.45	854 ± 370.5

n.d.: not determine.
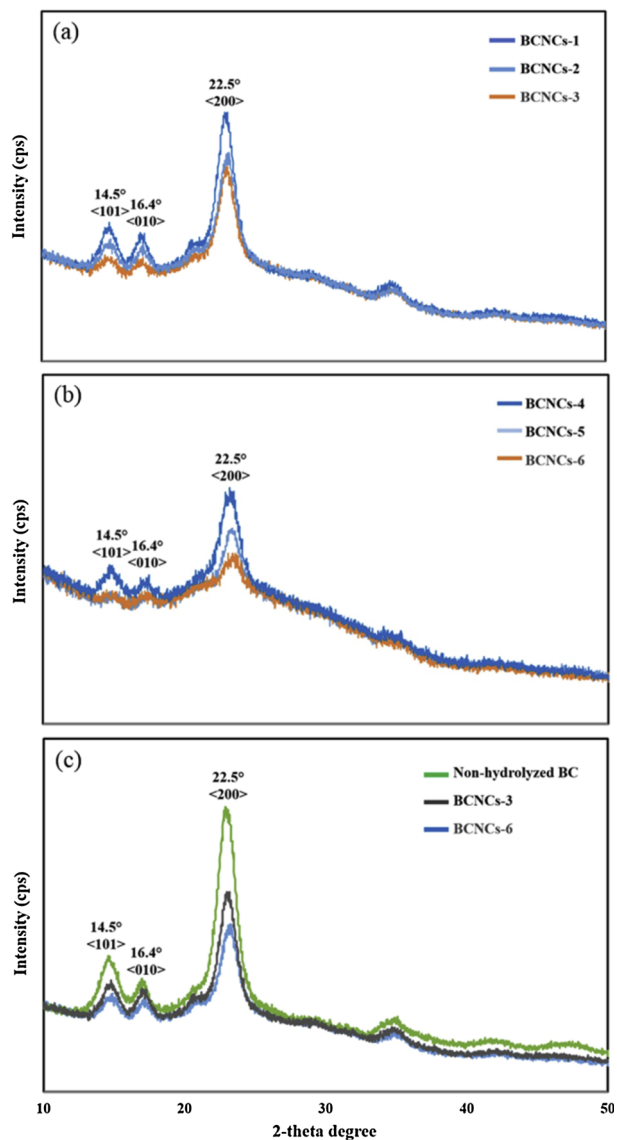
Fig. 4. XRD patterns obtained from HCl-hydrolyzed BC with hydrolysis time-varying at 4, 5, and 6 h (BCNCs-1 to 3) (a), XRD patterns obtained from H_2SO_4-hydrolyzed BC with hydrolysis time-varying at 1, 2, and 3 h (BCNCs-4 to 6) (b), XRD patterns obtained from non-hydrolyzed BC, BCNCs-3, and BCNCs-6 (c).

is a main factor that significantly influences the physical, structural and mechanical properties of materials. Therefore, the XRD patterns obtained from HCl-hydrolyzed BC samples with hydrolysis time-varying at 4, 5, and 6 h (BCNCs 1 to 3) (Fig. 4a), XRD patterns obtained from H_2SO_4-hydrolyzed BC samples with hydrolysis time-varying at 1, 2, and 3 h (BCNCs-4 to 6) (Fig. 4b), and XRD patterns obtained from pristine BC, BCNCs-3 and BCNCs-6 (Fig. 4c) were used to determine the percent crystallinity (Cr (%)) and the crystallite size (L_{hkl}) of pristine BC and all acid-hydrolyzed BCNCs. The results indicated that all BCNCs had a Cr (%) (85.4–90.2%) greater than pristine BC (81.1.%) (Table 1). The higher in crystallinity after acid hydrolysis reaction was because of a rapid and continuous decrease of the amorphous content, as this amorphous phase is to a higher degree accessible to acid penetration. The comparison of the Cr (%) of BCNCs-3 and BCNCs-6 (which differed in acid types and the reaction time), significant difference was detected. For BCNCs-6 (involving a higher reaction time), a decrease in the Cr (%) and the crystallite size was observed, possibly due to the harsh hydrolysis conditions, resulting in a probably change in the orientation of the BC main chains. Contrarily, BCNCs-3 showed a higher Cr (%) than the BCNCs obtained after acid hydrolysis H_2SO_4. From this, it was evident that H_2SO_4 involved in the integration structure of BC fiber bundles significantly influence the cleavage of covalent or glycosidic linkage/bonds, therefore generating smaller single crystallite size with higher amorphous contents. Additionally, the crystallite size (L_{hkl}) of pristine BC and all acid-hydrolyzed BCNCs were calculated from the XRD spectra by using the Scherrer equation (Singhsa et al., 2018a; Vasconcelos et al., 2017) (Table 1). The pristine BC showed the larger L_{hkl} (6.9 nm) than their nanocrystals. Compared with the BCNC-3 and BCNC-6 conditions, the nanocrystals obtained under time-varying hydrolysis conditions showed slight differences in the L_{hkl} values. The L_{hkl} was slightly decreased with increasing acid hydrolysis reaction time. The reduction in the L_{hkl} of acid-hydrolyzed BCNCs purposed that acid hydrolysis is tend to reducing the crystalline part of the original materials (Castro et al., 2011; Singhsa et al., 2018a). Thus, we conclude that the L_{hkl} of H_2SO_4-hydrolyzed BCNCs with the highest acid hydrolysis reaction time (BCNCs-6) were the smallest (4.6 nm) compared to other acid hydrolysis conditions; these results could confirm the high surface area of BCNCs are successfully developed by H_2SO_4 acid hydrolysis for increasing its dispersibility into other matrix materials as an excellent additive material, while maintaining the unique properties of pristine BC.

3.1.2. Hydrodynamic sizes and ζ-potential

The physicochemical characterization of pristine BC and BCNCs obtained through acid hydrolysis under different conditions (Table 1). For H_2SO_4 acid hydrolysis reaction, H_2SO_4 has the ability to esterify the hydroxyl (OH−) groups of cellulose with sulfate groups (−OSO_3−) to offer an acid half-ester or the so-called cellulose sulfate (sulfated cellulose) (Singhsa et al., 2018a), this is cause to generate negatively charged surface nanocrystals. Accordingly, the strong acid hydrolytic activity of H_2SO_4, the BCNCs prepared by H_2SO_4 hydrolysis had the smallest hydrodynamic sizes, which were 868.5, 861.8, and 854 d.nm for BCNCs-4, BCNCs-5, and BCNCs-6, respectively. Therefore, this helps to separate the coalescence of nanocrystals forced by hydrogen bonding, and then the consistent well-dispersed BCNCs suspension can

be received. In contrast, HCl has milder acid-hydrolysis reaction and basically promotes cellulose crystallites with native crystalline structures that have no evident of sulfate groups, resulting in the production of neutral nanocrystals. Therefore, the hydrodynamic sizes of the HCl-hydrolyzed BCNCs were larger, 1153, 1142, and 1122 d.nm for BCNCs-1, BCNCs-2, and BCNCs-3, respectively.

The zeta potential is commonly applied to indicate the presence of surface charges on any material that can be correlated to the zeta potential of the particles. In addition, zeta potential is important for a superior understanding on the character of the particle stability, and it has also been well-known that suspension particles with higher absolute values of the zeta potential have a tendency to be less aggregated by reason of high electrical repulsion among the particles (Elimelech, Nagai, Ko, & Ryan, 2000; Vasconcelos et al., 2017). Zeta potential values with a modulus with higher than 30 mV reflect good stability of a colloidal suspension (Vasconcelos et al., 2017). The all tested acid-hydrolysis reaction resulted in BCNCs suspensions with high zeta potential values, especially in H_2SO_4, confirming their remarkable stability. The nanocrystals had a highly negative surface-charge density because of the conjugated effect among sulfate groups ($-OSO_3-$) derived from esterification and the hydroxyl groups present on the BCNCs surface. Thus, the H_2SO_4-hydrolyzed BCNCs was modified with sulfate groups on their surface and became a highly negative sulfated BCNCs, resulting in the highly negative surface ζ-potential values of -33.5, -34.2, and -34.3 mV for BCNCs-4, BCNCs-5, and BCNCs-6, respectively. In contrast, HCl has milder acid-hydrolysis reaction, resulting in their ζ-potential values were insignificant negative compared to H_2SO_4-hydrolyzed BCNCs, about -21.5, -21.9, and -22.6 mV for BCNCs-1, BCNCs-2, and BCNCs-3, respectively. For HCl-hydrolyzed BCNCs, the presence of lower negative charges could be the reason of a significantly increased of oxidation of the BC main chains by reactive oxygen species throughout BC acid hydrolysis, causing negatively charged functional groups, such as for example, carboxylic groups on the surface of nanocrystals (Winter et al., 2010). Consequently, the remarkable hydrodynamic sizes and ζ-potential values of the H_2SO_4-hydrolyzed BCNCs was successfully developed for increasing its dispersibility on alginate-based film while maintaining the unique properties of pristine BC, thus preventing their aggregation, and also for increasing AgNPs dispersibility, leading AgNPs to be more possibility of access to H_2S gas.

3.1.3. Total specific surface area and micro-pore volume

The BET-adsorption isotherms curve of pristine BC, HCl-hydrolyzed BCNCs (BCNCs-3), and H_2SO_4-hydrolyzed BCNCs (BCNCs-6) were characterized (Fig. S2) in order to identify the total specific surface area, A_s (m^2/g) and micro-pore volume, V_m (cm^3(STP)/g) (Table 1). As a result of the strong acid hydrolytic activity, the BCNCs prepared by HCl and H_2SO_4 hydrolysis, we should expect an enlarged total specific surface. Comparing the A_s of pristine BC (3.1 m^2/g), BCNCs-3 (6.0 m^2/g), and BCNCs-6 (6.3 m^2/g), the highest of A_s were found in H_2SO_4-hydrolyzed BCNCs (BCNCs-6) and the lowest of A_s were found in pristine BC. The results of this measurement are closely linked with those of the ζ-potential analysis because the higher ζ-potential value that promotes the cellulose fibers to be less aggregated in order to increase A_s value. Moreover, the micro-pore volumes was investigated. Since the bacterial cellulose fibers have only rod-like or whisker-shaped particles, it was suggested that they are absolutely non-porous exhibiting only very small micro-pore volumes (Bismarck et al., 2002). Comparing the V_m of pristine BC (0.72 cm^3(STP)/g), BCNCs-3 (1.38 cm^3(STP)/g), and BCNCs-6 (1.45 cm^3(STP)/g), the highest of V_m were found in H_2SO_4-hydrolyzed BCNCs (BCNCs-6) and the lowest of A_s were found in pristine BC. It was found that the higher value in the V_m area and A_s were promoted by the de-aggregated cellulose fibers with highly negative surface charges. It is highly recommended that H_2SO_4-hydrolyzed BCNCs (BCNCs-6) could be used for increasing AgNPs dispersibility.

3.1.4. Identification of cellulosic fibres and cellulose I_α content (%)

The FTIR spectra of pristine BC, BCNCs-3, and BCNCs-6 (Fig. S3) showed typical cellulose vibration bands, such as 3313 cm^{-1} (stretching of O−H bonds), 1428 cm^{-1} (asymmetric angular deformation of C−H bonds), 1163 cm^{-1} (asymmetrical stretching of C−O−C glycoside bonds), 1110 cm^{-1} and 1059 cm^{-1} (stretching of C−OH and C−C−OH bonds in secondary and primary alcohols, respectively), 1024 cm^{-1} (C−O−C anti-symmetric stretching), 896 cm^{-1} (angular deformation of C−H bonds) (Vasconcelos et al., 2017), and $700-800\ cm^{-1}$ (H-bonding vibrations) (Szymańska-Chargot, Cybulska, & Zdunek, 2011). However, there was no evident IR peak of the 807 cm^{-1} band for C−S bond symmetric vibration of C−O−SO_3− groups, generated by ester-ification of H_2SO_4 acid-hydrolysis reaction by the reason of the small amount of the attached sulfate groups (Singhsa et al., 2018a). Normally, cellulosic materials are homogenous polycrystalline macromolecular compound, and it is consisted of crystalline (main ordered) and amorphous (less ordered) regions (Bi et al., 2014). Besides, it is recognized that the crystalline region of cellulose I is a compound of two distinct crystalline types: meta-stable state celluloses I_α (triclinic) and stable state celluloses I_β (monoclinic) (Ross, Mayer, & Benziman, 1991). The FT-IR spectroscopy was performed in order to identify the I_α content of bacterial cellulose samples that could be evaluated by the integrated intensities from the IR absorbencies at around 750 and 710 cm^{-1} (Fig. S4). Table 1 shows cellulose I_α content (%) of pristine BC and BCNCs obtained through acid hydrolysis under different conditions, with the values ranged from 92.3–90.1%. Hence, it is confirmed that the BC is rich cellulose I_α contents, whereas plant cellulose is rich in cellulose I_β (Atalla & Vanderhart, 1984). Comparing the I_α content (%) of pristine BC and all BCNCs conditions, the highest I_α content (92.3%) were found in H_2SO_4-hydrolyzed BCNCs (BCNCs-6) and the lowest of I_α content (90.1%) were found in pristine BC. Furthermore, these results were closely related to the I_α/I_β ratios obtained from XRD analysis. However, the I_α content (%) were not significantly different among samples in different conditions. It suggested that an increase of acid hydrolysis reaction time, types of acid and the esterification of sulfate groups could not significantly influence the I_α content (%) of bacterial cellulose.

3.2. Preparation of BCNCs based surface-loaded AgNPs and their properties

Accordingly, the previous results in Table 1, we found that suitable condition of acid hydrolysis reaction for preparing BCNCs with H_2SO_4 hydrolyzed BCNCs at 45 °C for 3 h (BCNCs-6) when compared to those with different conditions, results in the smallest hydrodynamic sizes (854 d.nm) the smallest crystallite sizes (4.6 nm), and the highest negative surface ζ-potential values (-34.3 mV); these results could confirm the high surface area and the high dispersibility by increasingly interacting with other materials.

3.2.1. Formation of AgNPs on BCNCs-6

By the immersion of BCNCs-6 in silver ion Ag^+ aqueous solutions using $Ag(NO_3)$ as Ag^+ precursors, the high surface of the several single fibers with three-dimensional network structure of the BCNCs-6, as shown in Fig. 2c, could allow Ag^+ ions to penetrate into the BCNCs-6 structure as long as the adsorption equilibrium is accomplished. According to, Ag^+ ions is impregnated and loaded onto the stable absorption site via electrostatic repulsive interaction between Ag^+ ions and lone pair electrons of OH (hydroxyl) groups on the surface of BCNCs-6 nanofibers (Azizi, Ahmad, Mahdavi, & Abdolmohammadi, 2013; Janpetch et al., 2016), as shown in chemical Eqs. (9)–(12):
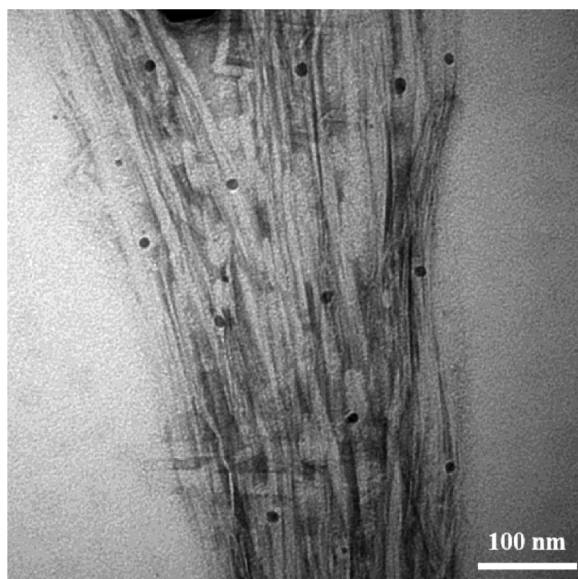
$$4Ag(NO_3)\ (s) + 2H_2O \rightarrow 4Ag^+ + 4HNO_3 + O_2 \tag{9}$$

$$Ag^+ + \text{surface of BCNCs} \rightarrow Ag^{+\cdot\cdot}\ \cdot BCNCs \tag{10}$$

$$Ag^{+\cdot\cdot}\ \cdot BCNCs + OH- \rightarrow AgOH..\ .\ BCNCs \tag{11}$$

P. Sukhavattanakul and H. Manuspiya

Fig. 5. TEM micrographs of BCNCs-6 based surface-loaded AgNPs. TEM, scale markers correspond to 100 nm.

$$AgOH.. . BCNCs \rightarrow AgNPs.. . BCNCs + H_2O \qquad (12)$$

After the stable absorption site via electrostatic repulsive interaction of Ag^+ ions on BCNCs fibers, the Ag^+ saturated-BCNCs were ion-reduced and transformed to silver nanoparticles (AgNPs) deposited on the surface of BCNCs fibers via the chemical reaction with OH- from NH₄OH (Janpetch et al., 2016; Li, Shi, Zhong, & Yin, 1999; Yang, Zhu, Liu, Chen, & Ma, 2008), as shown in chemical Eq. (13)

$$2OH- + 2Ag^+ \rightarrow AgO + AgNPs.. . BCNCs + H_2O \qquad (13)$$
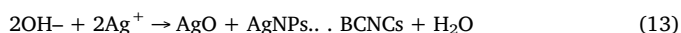
Consequently, morphological properties of the obtained dry BCNCs–AgNPs samples were analyzed.

3.2.2. Microstructural characteristics of BCNCs–AgNPs

Morphological analysis of the obtained BCNCs–AgNPs samples by TEM micrograph (Fig. 5), the average size and shape of the AgNPs were approximately in the range from 1 nm to 10 nm although some agglomeration was also present. The results from these micrographs could confirm the well-dispersed of AgNPs with the high surface area of BCNCs-6 by increasingly interacting surface between each other.

3.2.3. Elemental analysis of BCNCs–AgNPs

The elemental composition of BCNCs-AgNPs was determined by the energy-dispersive X-ray (EDX) analysis, the samples of BCNCs-AgNPs were coated with platinum (Pt) by ion sputtering. The EDX images in Fig. S5a and b were analyzed by X-ray dot mapping mode and the EDX images in Fig. S5c was taken by using element identification mode. In Fig. S5c, EDX images of BCNCs–AgNPs sporadically surface-loaded by AgNPs with which they closely interact to BCNCs-6 to form a physical adsorption. There are significant peaks of the Ag element, which belong to AgNPs is loaded on the surface of BCNCs-6 with homogenously dispersed, as shown in Fig. S5b. Thus, it is confirmed that the hybridization of AgNPs and BCNCs by using the chemical reducing reagent under ultrasonic treatment solution could accomplish the hybridization by physical adsorption of AgNPs on BCNCs's surface. They also exhibit the rather high peak of the C and O element, which are a general component of BCNCs and other cellulosic material.

3.3. Preparation of hybrid BCNCs–AgNPs/alginate–MoO₃NPs film and their properties

3.3.1. Formation of hybrid BCNCs–AgNPs/alginate–MoO₃NPs film

The demonstration of the hybrid material of BCNCs–AgNPs/ alginate–MoO₃NPs prepared by physical adsorption techniques and its film form are shown in Fig. 6a and b. The hybrid of the BCNCs–AgNPs/ alginate–MoO₃NPs in the form of solution and film can be both in Mo (V)O₃ (Mo^{5+}) and Mo(VI)O₃ (Mo^{6+}) characterized by x-ray photoelectron spectroscopy (XPS) technique.

The preparation of Mo(VI)O₃NPs solution with ultrapure water Eq. (14), $Mo^{5+}\bullet H_2O$ and $Mo^{6+}\bullet H_2O$ were occurred without separation of the new phase. The two water molecules in $Mo^{5+}\bullet H_2O$ and $Mo^{6+}\bullet H_2O$
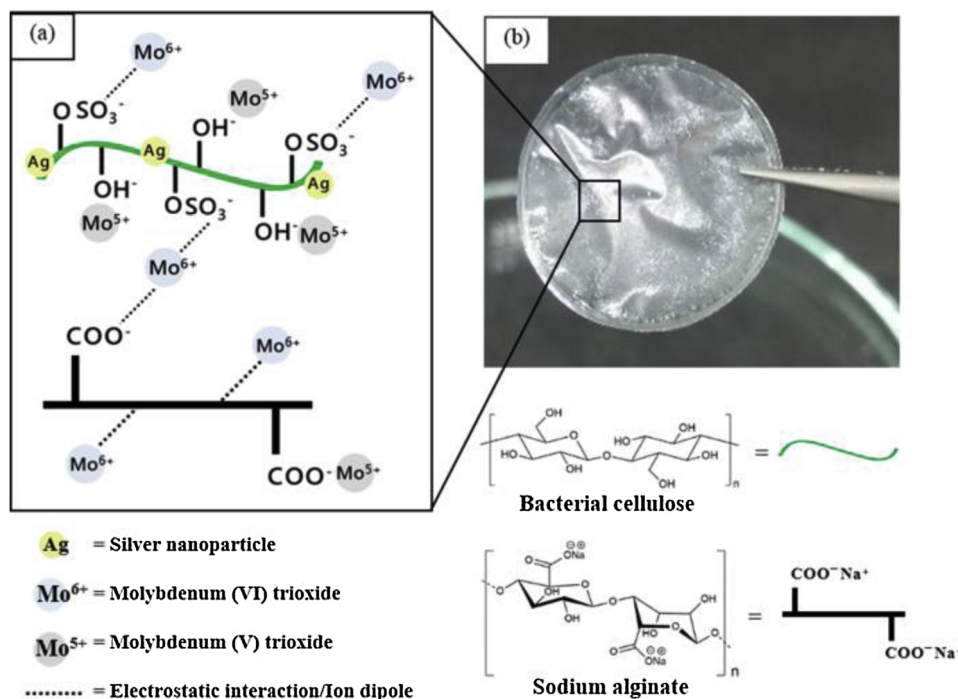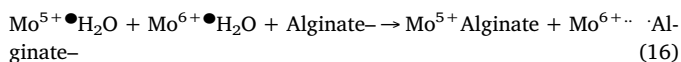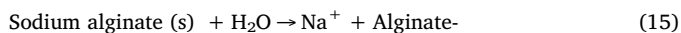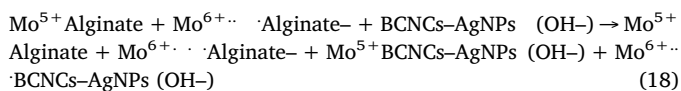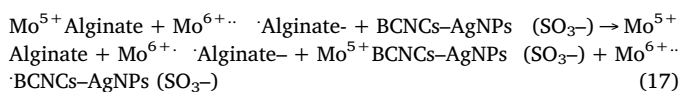

Fig. 6. Schematic demonstration of the hybrid material of BCNCs–AgNPs/ alginate–MoO₃NPs prepared by physical adsorption techniques (a) and its film form (b).

P. Sukhavattanakul and H. Manuspiya

are different bonded types, depending on the oxidation state of Mo. For $Mo^{5+} \cdot H_2O$, in addition of oxygens, is coordinated to Mo atoms in one layer to oxygen ions in the next layer, and for the $Mo^{6+} \cdot H_2O$ is held by hydrogen bonding in between the layers of MoO_3 (Günter, 1972). By the immersion of sodium alginate in the $Mo(VI)O_3NPs$ solution, the carboxylate side groups with several of the negative charges of alginate Eq. (15), is highly reactive to cations of Mo^{5+} to form Mo^{5+}Alginate, and also to electrostatic repulsive interaction with Mo^{6+} to form $Mo^{6+} \cdot \cdot$Alginate– Eq. (16).

$$Mo(VI)O_3NPs\ (s) + 2H_2O \rightarrow Mo^{5+} \cdot H_2O + Mo^{6+} \cdot H_2O \quad (14)$$

$$Sodium\ alginate\ (s)\ + H_2O \rightarrow Na^+ + Alginate- \quad (15)$$

$$Mo^{5+} \cdot H_2O + Mo^{6+} \cdot H_2O + Alginate– \rightarrow Mo^{5+}Alginate + Mo^{6+} \cdot \cdot Alginate– \quad (16)$$

By hybridizing the dried BCNCs–AgNPs to alginate–MoO_3NPs solution, there are two different types of surface negative charges on the surface of BCNCs–AgNPs: (i) from sulfate groups (SO_3–); and (ii) from hydroxyl groups (OH–), and thus causing different interactions with Mo and alginate (Eqs. (17)–(18)).

$$Mo^{5+}Alginate + Mo^{6+} \cdot \cdot Alginate- + BCNCs–AgNPs\ (SO_3–) \rightarrow Mo^{5+}Alginate + Mo^{6+} \cdot Alginate– + Mo^{5+}BCNCs–AgNPs\ (SO_3–) + Mo^{6+} \cdot \cdot BCNCs–AgNPs\ (SO_3–) \quad (17)$$

$$Mo^{5+}Alginate + Mo^{6+} \cdot \cdot Alginate– + BCNCs–AgNPs\ (OH–) \rightarrow Mo^{5+}Alginate + Mo^{6+} \cdot \cdot Alginate– + Mo^{5+}BCNCs–AgNPs\ (OH–) + Mo^{6+} \cdot \cdot BCNCs–AgNPs\ (OH–) \quad (18)$$

Consequently, properties of the obtained hybrid BCNCs–AgNPs/ alginate–MoO_3NPs film samples were analyzed and H_2S gas sensor ability was characterized using XPS with H_2S gas exposure experiment.

3.3.2. Physical appearances of the film

The hybrid BCNCs–AgNPs/alginate–MoO_3NPs films were visually homogeneous with no air bubbles, wrinkles, snags, or brittle areas and were easily manipulatable and moderately flexible. The appearance of the film was not significantly affected by the addition of bacterial cellulose and metal nanoparticles at a 50 mM of MoO_3 solution and 0.1 dry wt% of BCNCs–AgNPs except for the film color which was changed very little from its initial alginate film (transparent white color). The transparency of the film was evaluated visually and photographed (Fig. 6b), showing the development of a light greyish-white color, depending on the MoO_3 content. The average thickness of the film measured by a micrometer was approximately 90 μm.

3.3.3. Identification of alginate and MoO_3NPs

FTIR analysis of the BCNCs-6, BCNCs-6–AgNPs/alginate–MoO_3NPs film, and alginate film attempted to characterize the hybridization of BCNCs-6–AgNPs and alginate–MoO_3NPs by distinguishing the infrared (IR) bands and vibration shifts related to the BCNCs-alginate and MoO_3NPs–alginate interactions (Fig. S6). The characteristic peak of alginate polysaccharide vibration bands, such as the peak at 1602 cm^{-1} (−C=O carbonyl bonds), 1424 and 1024 cm^{-1} in both alginate and BCNCs were assigned to (−COO and −C−O carboxyl stretching bands) (Deepa et al., 2016), 3313 cm^{-1} (−O−H aliphatic chain stretching vibrations), and 2930 cm^{-1} (−C−H aliphatic chain stretching vibrations). For the hybrid BCNCs-6–AgNPs/alginate–MoO_3NPs film, the Mo=O bonding vibration bands is clearly shown as a sharp band centered at about 950 cm^{-1}, and characteristic peaks were present in the $953 - 957$ cm^{-1} range, which can be determined to the stretching mode of the terminal Mo=O group (Afsharpour, Mahjoub, & Amini, 2009; Bhattacharya, Dinda, & Saha, 2015) and 865 cm^{-1} are assigned to the Mo–O–Mo stretching vibrations of MoO_3 (Bhattacharya et al., 2015). Some reports showed a high peak intensity of terminal M=O bonds (993 cm^{-1} and 817 cm^{-1}) presents a large oxygen vacancy (Bhattacharya et al., 2015). Some differences can be observed after MoO_3NPs addition

into the alginate matrix. Consequently, occurrence of the peak with a sharp band centered at about 950 cm^{-1} and 865 cm^{-1} were observed as the MoO_3NPs was incorporated into the alginate matrix. These results can represent the existence of the ionic bonding and electrostatic repulsive interaction between the alginate and MoO_3NPs. MoO_3NPs in the form of $Mo(V)O_3$ (Mo^{5+}) are formed an ionic bonded with carboxylic acid groups (−COO−) on the alginate chain, and MoO_3NPs in the form of $Mo(VI)O_3$ (Mo^{6+}) are physically adsorbed on both in the alginate chain and sulfate groups (−OSO_3−) on the BCNCs's surface by electrostatic interaction.

3.3.4. Elemental analysis of BCNCs–AgNPs/alginate–MoO_3NPs film

The elemental composition of the hybrid BCNCs–AgNPs/ alginate–MoO_3NPs film was determined by EDX analysis, the film sample was coated with platinum (Pt) by

ion sputtering. The EDX images in Fig. S7a–c were analyzed by X-ray dot mapping mode and the EDX images in Fig. S7d was taken by using element identification mode. In Fig. S7d, EDX images of the hybrid BCNCs–AgNPs/alginate–MoO_3NPs film based on the alginate matrix, sporadically hybridized by MoO_3NPs and BCNCs–AgNPs with which they closely interact to alginate to form a physical adsorption. There are significant peaks of the Ag element, which belong to AgNPs are loaded on the surface of BCNCs-6 with homogenously dispersed, as shown in Fig. S7b. Besides, the significant peaks of the Mo element, which belong to MoO_3NPs are loaded on the alginate with homogenously dispersed, as shown in Fig. S7c. Thus, it is confirmed that the hybridization of: (i) alginate and MoO_3NPs by using ultrasonic treatment solution could accomplish the hybridization by physical adsorption by covalent and ionic bonds of MoO_3NPs with carboxylic acid groups (−COO−) on the alginate chain; and (ii) BCNCs–AgNPs by using the chemical reducing reagent under ultrasonic treatment solution could accomplish the hybridization by physical adsorption of AgNPs on BCNCs's surface. They also exhibit the rather high peak of the C and O element, which are a general component of alginate polysaccharide, BCNCs and other cellulosic material.

3.4. H_2S gas exposure experiment

3.4.1. H_2S gas sensor ability of hybrid BCNCs–AgNPs/alginate–MoO_3NPs film

For the H_2S gas exposure experiment, the demonstration of the in-house H_2S gas preparation and H_2S gas exposure experiment of hybrid BCNCs–AgNPs/alginate–MoO_3NPs film is shown in Fig. S8. The concentration of H_2S gas was calculated to be approximately 1400 ppm in the tightly septum-capped glass bottle and then was diluted 100 times by displaced 5 mL of the H_2S gas using syringe plunger to each of the film sample bottles with the same bottle volume. Finally, each of the film sample bottles was reached the H_2S gas in concentration of approximately 14 ppm and leave them with gas exposure time-varying for 5 min, 1 h, and 24 h.

The fast H_2S gas sensor of the hybrid BCNCs–AgNPs/ alginate–MoO_3NPs film would be highly useful for a low concentration of H_2S at 14 ppm, in which increase of the Mo sub-oxide color intensity according to the increase of H_2S gas exposure time (Fig. 7a–d). The change in color of the hybrid BCNCs–AgNPs/alginate–MoO_3NPs film
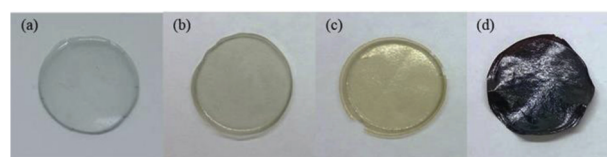

Fig. 7. H_2S gas exposure of hybrid BCNCs–AgNPs/alginate–MoO_3NPs film; before exposing to H_2S gas (a), after exposing to 14 ppm of H_2S for 5 min (b), 1 h (c), and 24 h (d).
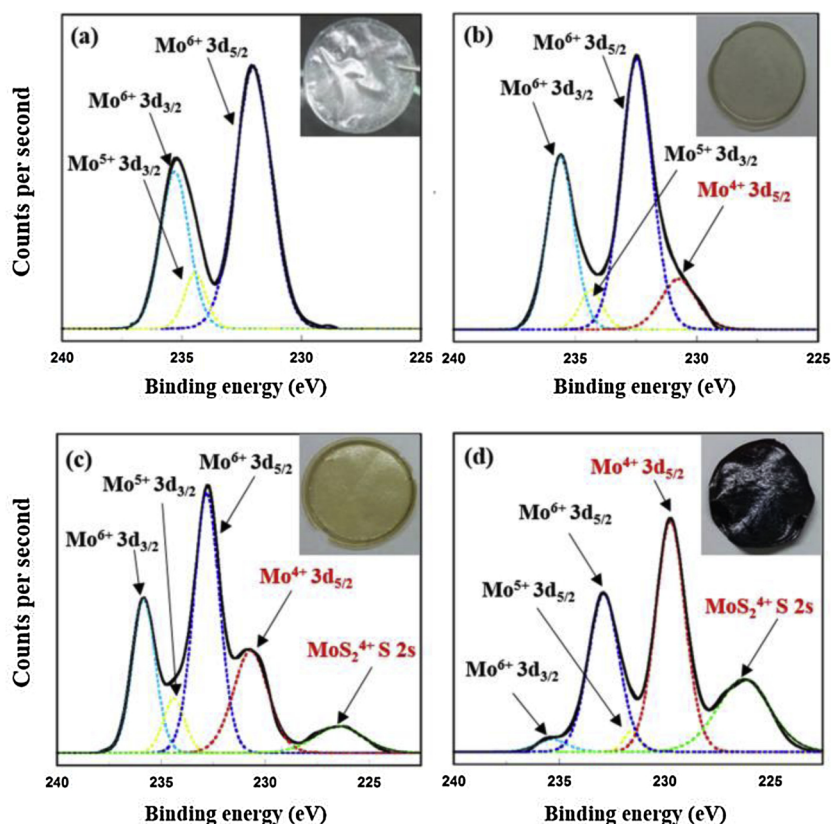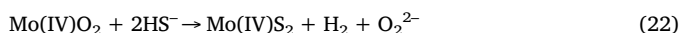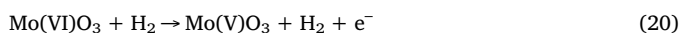
Fig. 8. XPS spectra of the BCNCs–AgNPs/alginate–MoO$_3$NPs films in order to examine the valence states of the Mo 3d, 5d, and 2 s region for Mob; before exposing to H$_2$S gas (a), after exposing to 5 mL of H$_2$S gas for 5 min (b), 1 h (c), and 24 h (d).

from transparent light-grey to opaque dark brown-black can be assigned to the conversion of Ag to Ag$_2$S to produce atomic H, and then the Mo to from MoO$_3$NPs are readily reduced to a colored sub-oxide by atomic H.

3.4.2. Mechanism of H$_2$S sensing

Pristine MoO$_3$ consists of Mo(VI)O$_3$(Mo^{6+}) forming the conduction bands and O^{2-} forming the valence bands (Borgschulte et al., 2017) can be assigned to Mo^{6+} 3d$_{5/2}$ and Mo^{6+} 3d$_{3/2}$, respectively (Gong & Haur, 2017; Ji et al., 2013). The first reaction is believed to occur at the HS– adsorbed on the AgNPs of the well-dispersed BCNCs–AgNPs to readily form Ag$_2$S and promptly generated H$_2$. Next, the intercalation of H$_2$ into MoO$_3$ by the vicinity of H$_2$ to oxygen without alteration of the structural motif apart from few increase of the cell volume (Borgschulte et al., 2017), and water is formed at longer gas exposure time. The dissociation of hydrogen molecule from the reaction of AgNPs and H$_2$S gas on oxide surfaces of MoO$_3$NPs in the film, which decomposes into MoO$_2^{+1/2}$ and H$_2$O by the fast decrease of Mo oxidation state from Mo^{6+} into Mo^{5+}, slowly forms Mo^{4+} states, forms a very low-intensity MoS$_2^{4+}$ at exposure time of 1 h, and forms a low-intensity MoS$_2^{4+}$ at exposure time of 24 h. Besides, the increase of AgNPs dispersibility by well-dispersed BCNCs–AgNPs in alginate–MoO$_3$ matrix phase, leading AgNPs to be more possibility of access to H$_2$S gas. The Mo(IV)S$_2$(Mo^{4+}) is considerably increased due to the loss of O$_2$, depending on gas exposure time of sampling. These conversion can be described by the chemical reactions as shown in chemical Eqs. (19)–(22):

$$8Ag + 4HS^- \rightarrow 4Ag_2S + 2H_2 + 4e^- \tag{19}$$

$$Mo(VI)O_3 + H_2 \rightarrow Mo(V)O_3 + H_2 + e^- \tag{20}$$

$$Mo(VI)O_3 + H_2 \rightarrow Mo(IV)O_2 + H_2O \tag{21}$$

$$Mo(IV)O_2 + 2HS^- \rightarrow Mo(IV)S_2 + H_2 + O_2^{2-} \tag{22}$$

The rate of reaction increases with the increase in gas exposure time. These mechanism fully support the H$_2$S gas sensor from the hybrid BCNCs–AgNPs/alginate–MoO$_3$NPs film by this gas exposure experiment.

3.4.3. XPS measurement

H$_2$S gas sensing characteristics of the films were examined from XPS spectrogram. A high-resolution XPS measurement was carried out in order to examine the surface chemical composition and the oxidation states of Mo. Fig. 8 shows the XPS spectra of the hybrid BCNCs–AgNPs/ alginate–MoO$_3$NPs films in order to examine the oxidation states of the Mo 3d, 5d, and 2 s region for Mo. According to the XPS spectra, all peak positions for Mo with different oxidation state are shown in the Table S3. The peaks at 232.8 and 235.9 eV, characteristic of MoO$_3$, can be assigned to Mo^{6+} 3d$_{5/2}$ and Mo^{6+} 3d$_{3/2}$, respectively (Ji et al., 2013). Under the H$_2$S gas exposure, the peak intensity of Mo^{5+} 3d$_{5/2}$, Mo^{6+} 3d$_{3/2}$, and Mo^{6+} 3d$_{5/2}$ XPS spectra (Fig. 8b–d) are prone to be reduced especially for 24 h, indicating a significant amount of Mo^{6+} in MoO$_3$ has been reduced to sub-oxide state to promote the change in color of the film.

The low energy peak at 229.8 eV can be observed and assigned to Mo^{4+} 3d$_{5/2}$ by reason of the reduction that occurred after H$_2$S gas exposure for 5 min, and the peak intensity is considerably increased at gas exposure for 1 h and 24 h, respectively. The signals from MoO$_3$ under gas exposure is considered to be along with the conversion that described by the chemical reactions as shown in chemical Eqs. (19)–(22).

For gas exposure at 24 h, the peak intensity at 229.8 eV (Mo^{4+} 3d$_{5/2}$) and 226.25 eV (MoS$_2^{4+}$ S 2 s) are much stronger than that of pristine MoO$_3$, indicating that on the MoO$_3$NPs surface the relative concentration of Mo^{4+} is higher than that of MoO$_3$ and the oxidation state of Mo is lower. The peak areas of Mo^{4+}/Mo^{6+} ratio from XPS spectra are determined to be 0.136, 0.477, and 2.037 for H$_2$S gas exposure time for

5 min, 1 h, and 24 h, respectively as shown in Table S4.

The ratio is determined based on: (i) the oxidation state or valence state of MoO_3 after losing the O molecule by H_2 intercalation (Mo(IV) $O_2(Mo^{4+})$); and (ii) the oxidation state of pristine MoO_3 (Mo(VI) $O_3(Mo^{6+})$). Thus, the conversion of Mo^{6+} to Mo^{4+} is depend on gas exposure time with the slower increase of the ratio value due to some limitation of Mo oxide surfaces for H_2 intercalation.

4. Conclusion

In this work, BC was successfully produced by bacterial strain of *K. xylinus* under static culture with average yield was 2.25 g/L of culture. The acid conditions profoundly influenced the physical properties of nanocrystals including the morphology, hydrodynamic size, ζ-potential, crystallite size, and CI. Accordingly, BCNCs was successfully achieved by acid hydrolysis under various acid conditions, namely, HCl, H_2SO_4 with time-varying. Resulting in H_2SO_4 acid-hydrolyzed BCNCs (BCNCs-6) were evaluated for their highest surface area (6.3 m^2/g) for interaction with metallic nanoparticles with the smallest crystallite size (4.6 nm) and hydrodynamic size (854 d.nm) with the most remarkable ζ-potential value (-34.3 eV) for negative surface charge. Thus, BCNCs-6 was selected for the study of BCNCs surface-loaded AgNPs and then hybridized with alginate-MoO_3NPs by physical adsorption under ultrasonic treatment to get film structure for H_2S gas sensor ability. Thus, the high surface area of BCNCs increase its dispersibility on alginate-based film while maintaining the unique properties of pristine BC, thus preventing their aggregation, and also for increasing AgNPs dispersibility, leading AgNPs to be more possibility of access to H_2S gas. H_2S gas with concentration 14 ppm, have been utilized for the measurements. The hybrid film of BCNCs–AgNPs/alginate–MoO_3NPs was successfully developed for H_2S gas sensor by reason of a change in Mo oxidation state and the reduction mechanism by atomic hydrogen intercalating of MoO_3NPs on the film. The Mo oxidation state on the film under H_2S gas exposure can be Mo(IV)$O_3(Mo^{4+})$, Mo(V)$O_3(Mo^{5+})$, and Mo(VI)O_3 (Mo^{6+}) examined from XPS spectrogram. The film color are changed from transparent light greyish-white to opaque dark brown-black indicated the dissociation of hydrogen molecule from the reaction of AgNPs and H_2S gas on oxide surfaces, which decomposes into $MoO_2^{+1/2}$ and H_2O by the fast decrease of Mo oxidation state from Mo^{6+} into Mo^{5+}, slowly forms Mo^{4+} states, forms a very low-intensity MoS_2^{4+} at exposure time of 1 h, and forms a low-intensity MoS_2^{4+} at exposure time of 24 h. The color intensity is gradually increased according to the increase of exposure time. Consequently, this study could provide useful information about the preparation of rod-like BCNCs from BC produced by *K. Xylinus* strain under static culture, surface-loaded with metal nanoparticles, and hybrid with alginate–MoO_3 to reach H_2S gas sensor ability, in addition to rendering the properties of nanocrystals in accordance with the desired applications.

Acknowledgements

Appendix A. Supplementary data

Supplementary material related to this article can be found, in the online version, at doi:https://doi.org/10.1016/j.carbpol.2019.115566.

References

Afsharpour, M., Mahjoub, A., & Amini, M. M. (2009). Synthesis of molybdenum oxide nanohybrids as efficient catalysts in oxidation of alcohols. *Journal of Inorganic and Organometallic Polymers and Materials, 19*.

Ashjaran, A., Yazdanshenas, M. E., Rashidi, A., Khajavi, R., & Rezaee, A. (2013). Overview of bio nanofabric from bacterial cellulose. *Journal of the Textile Institute, 104*(2), 121–131.

Atalla, R. H., & Vanderhart, D. L. (1984). Native cellulose: A composite of two distinct crystalline forms. *Science, 223*(4633), 283–285.

Azizi, S., Ahmad, M., Mahdavi, M., & Abdolmohammadi, S. (2013). Preparation, characterization, and antimicrobial activities of ZnO nanoparticles/cellulose nanocrystal nanocomposites. *BioResources, 8*.

Bhattacharya, S., Dinda, D., & Saha, S. K. (2015). Role of trap states on storage capacity in a graphene/MoO3 2D electrode material. *Journal of Physics D: Applied Physics, 48*.

Bi, J. C., Liu, S. X., Li, C. F., Li, J., Liu, L. X., Deng, J., ... Yang, Y. C. (2014). Morphology and structure characterization of bacterial celluloses produced by different strains in agitated culture. *Journal of Applied Microbiology, 117*(5), 1305–1311.

Bismarck, A., Aranberri, I., Springer, J., Lampke, T., Wielage, B., Stamboulis, A., ... Limbach, H.-H. (2002). Surface characterization of flax, hemp and cellulose fibers; surface properties and the water uptake behavior. *Polymer Composites, 23*, 872–894.

Borgschulte, A., Sambalova, O., Delmelle, R., Jenatsch, S., Hany, R., & Nüesch, F. (2017). Hydrogen reduction of molybdenum oxide at room temperature. *Scientific Reports, 7*, 40761.

Brockgreitens, J., & Abbas, A. (2016). Responsive food packaging: Recent progress and technological prospects. *Comprehensive Reviews in Food Science and Food Safety, 15*(1), 3–15.

Brunauer, S., Emmett, P. H., & Teller, E. (1938). Adsorption of gases in multimolecular layers. *Journal of the American Chemical Society, 60*(2), 309–319.

Cai, Z., & Kim, J. (2010). Bacterial cellulose/poly(ethylene glycol) composite: Characterization and first evaluation of biocompatibility. *Cellulose, 17*(1), 83–91.

Carpenter, T. S., Rosolina, S. M., & Xue, Z.-L. (2017). Quantitative, colorimetric paper probe for hydrogen sulfide gas. *Sensors and Actuators B, Chemical, 253*, 846–851.

Castro, C., Zuluaga, R., Putaux, J.-L., Caro, G., Mondragon, I., & Gañán, P. (2011). Structural characterization of bacterial cellulose produced by Gluconacetobacter swingsii sp. from Colombian agroindustrial wastes. *Carbohydrate Polymers, 84*(1), 96–102.

Chen, J., Wang, K., Hartman, L., & Zhou, W. (2008). H2S detection by vertically aligned CuO nanowire array sensors. *The Journal of Physical Chemistry C, 112*(41), 16017–16021.

Chen, R., Morris, H. R., & Whitmore, P. M. (2013). Fast detection of hydrogen sulfide gas in the ppmv range with silver nanoparticle films at ambient conditions. *Sensors and Actuators B, Chemical, 186*, 431–438.

Choudhary, M., Singh, N. K., Mishra, V. N., & Dwivedi, R. (2013). Selective detection of hydrogen sulfide using copper oxide-doped tin oxide based thick film sensor array. *Materials Chemistry and Physics, 142*(1), 370–380.

Coombs, C. E. O., Holman, B. W. B., Friend, M. A., & Hopkins, D. L. (2017). Long-term red meat preservation using chilled and frozen storage combinations: A review. *Meat Science, 125*(Supplement C), 84–94.

Corrêa, A. C., de Morais Teixeira, E., Pessan, L. A., & Mattoso, L. H. C. (2010). Cellulose nanofibers from curaua fibers. *Cellulose, 17*(6), 1183–1192.

Deepa, B., Abraham, E., Pothan, L. A., Cordeiro, N., Faria, M., & Thomas, S. (2016). Biodegradable nanocomposite films based on sodium alginate and cellulose nanofibrils. *Materials, 9*(1), 50.

Dufresne, A. (2012). *Nanocellulose: From nature to high performance tailored materials*. De Gruyter.

Elimelech, M., Nagai, M., Ko, C.-H., & Ryan, J. N. (2000). Relative insignificance of mineral grain zeta potential to colloid transport in geochemically heterogeneous porous media. *Environmental Science & Technology, 34*(11), 2143–2148.

Foresti, M. L., Vázquez, A., & Boury, B. (2017). Applications of bacterial cellulose as precursor of carbon and composites with metal oxide, metal sulfide and metal nanoparticles: A review of recent advances. *Carbohydrate Polymers, 157*, 447–467.

Fu, L., Zhang, J., & Yang, G. (2013). Present status and applications of bacterial cellulose-based materials for skin tissue repair. *Carbohydrate Polymers, 92*(2), 1432–1442.

Gahlaut, S. K., Yadav, K., Sharan, C., & Singh, J. P. (2017). Quick and selective dual mode detection of H2S gas by mobile app employing silver nanorods array. *Analytical Chemistry, 89*(24), 13582–13588.

George, J., Ramana, K. V., Bawa, A. S., & Siddaramaiah (2011). Bacterial cellulose nanocrystals exhibiting high thermal stability and their polymer nanocomposites. *International Journal of Biological Macromolecules, 48*(1), 50–57.

Gonçalves, L. F. F. F., Silva, C. J. R., Kanodarwala, F. K., Stride, J. A., Pereira, M. R., & Gomes, M. J. M. (2013). Synthesis and characterization of organic–inorganic hybrid materials prepared by sol–gel and containing ZnxCd1 − xS nanoparticles prepared by a colloidal method. *Journal of Luminescence, 144*, 203–211.

Gong, L., & Haur, S. C. (2017). On demand rapid patterning of colored amorphous molybdenum oxide painted via a focused laser beam. *Journal of Materials Chemistry C, 5*.

Günter, J. R. (1972). Topotactic dehydration of molybdenum trioxide-hydrates. *Journal of Solid State Chemistry, 5*(3), 354–359.

Infahsaeng, Y., & Ummartyotin, S. (2017). Investigation on structural properties of Al-substituted ZnS particle prepared from wet chemical synthetic route. *Results in Physics, 7*, 1245–1251.

Janpetch, N., Saito, N., & Rujiravanit, R. (2016). Fabrication of bacterial cellulose-ZnO composite via solution plasma process for antibacterial applications. *Carbohydrate Polymers, 148*, 335–344.

Ji, W., Shen, R., Yang, R., Yu, G., Guo, X., Peng, L., ... Ding, W. (2013). Partially nitrided

molybdenum trioxide with promoted performance as an anode material for lithium-ion batteries. *Journal of Materials Chemistry A, 2*.

Jozala, A. F., de Lencastre-Novaes, L. C., Lopes, A. M., de Carvalho Santos-Ebinuma, V., Mazzola, P. G., Pessoa-Jr, A., ... Chaud, M. V. (2016). Bacterial nanocellulose production and application: A 10-year overview. *Applied Microbiology and Biotechnology, 100*(5), 2063–2072.

Kabcum, S., Tammanoon, N., Wisitsoraat, A., Tuantranont, A., Phanichphant, S., & Liewhiran, C. (2016). Role of molybdenum substitutional dopants on H2S-sensing enhancement of flame-spray-made SnO2 nanoparticulate thick films. *Sensors and Actuators B, Chemical, 235*, 678–690.

Kersen, Ü., & Holappa, L. (2006). Surface characterization and H2S-sensing potential of iron molybdate particles produced by supercritical solvothermal method and subsequent oxidation. *Applied Physics A, 85*(4), 431–436.

Keshk, S. (2014). Bacterial cellulose production and its industrial applications. *Journal of Bioprocessing & Biotechniques, 4*.

Kurosumi, A., Sasaki, C., Yamashita, Y., & Nakamura, Y. (2009). Utilization of various fruit juices as carbon source for production of bacterial cellulose by Acetobacter xylinum NBRC 13693. *Carbohydrate Polymers, 76*(2), 333–335.

Lee, C. M., Gu, J., Kafle, K., Catchmark, J., & Kim, S. H. (2015). Cellulose produced by Gluconacetobacter xylinus strains ATCC 53524 and ATCC 23768: Pellicle formation, post-synthesis aggregation and fiber density. *Carbohydrate Polymers, 133*, 270–276.

Li, H.-Y., Huang, L., Wang, X.-X., Lee, C.-S., Yoon, J.-W., Zhou, J., ... Lee, J.-H. (2017). Molybdenum trioxide nanopaper as a dual gas sensor for detecting trimethylamine and hydrogen sulfide. *RSC Advances, 7*(7), 3680–3685.

Li, W.-J., Shi, E.-W., Zhong, W.-Z., & Yin, Z.-W. (1999). Growth mechanism and growth habit of oxide crystals. *Journal of Crystal Growth, 203*(1), 186–196.

Lin, H.-M., Hsu, C.-M., Yang, H.-Y., Lee, P.-Y., & Yang, C.-C. (1994). Nanocrystalline WO3-based H2S sensors. *Sensors and Actuators B, Chemical, 22*(1), 63–68.

Lin, N., & Dufresne, A. (2014). Nanocellulose in biomedicine: Current status and future prospect. *European Polymer Journal, 59*(Supplement C), 302–325.

Lin, N., Huang, J., & Dufresne, A. (2012). Preparation, properties and applications of polysaccharide nanocrystals in advanced functional nanomaterials: A review. *Nanoscale, 4*.

MalekAlaie, M., Jahangiri, M., Rashidi, A. M., HaghighiAsl, A., & Izadi, N. (2015). Selective hydrogen sulfide (H2S) sensors based on molybdenum trioxide (MoO3) nanoparticle decorated reduced graphene oxide. *Materials Science in Semiconductor Processing, 38*, 93–100.

Malone Rubright, S. L., Pearce, L. L., & Peterson, J. (2017). Environmental toxicology of hydrogen sulfide. *Nitric Oxide, 71*, 1–13.

Maneerung, T., Tokura, S., & Rujiravanit, R. (2008). Impregnation of silver nanoparticles into bacterial cellulose for antimicrobial wound dressing. *Carbohydrate Polymers, 72*(1), 43–51.

Martínez-Sanz, M., Lopez-Rubio, A., & Lagaron, J. M. (2011). Optimization of the nanofabrication by acid hydrolysis of bacterial cellulose nanowhiskers. *Carbohydrate Polymers, 85*(1), 228–236.

McMillin, K. W. (2017). Advancements in meat packaging. *Meat Science, 132*, 153–162.

Mohebi, E., & Marquez, L. (2015). Intelligent packaging in meat industry: An overview of existing solutions. *Journal of Food Science and Technology, 52*(7), 3947–3964.

Murphy, K. M., O'Grady, M. N., & Kerry, J. P. (2013). Effect of varying the gas headspace to meat ratio on the quality and shelf-life of beef steaks packaged in high oxygen modified atmosphere packs. *Meat Science, 94*(4), 447–454.

Pandey, S. K., Kim, K.-H., & Tang, K.-T. (2012). A review of sensor-based methods for monitoring hydrogen sulfide. *TrAC Trends in Analytical Chemistry, 32*, 87–99.

Remenant, B., Jaffrès, E., Dousset, X., Pilet, M.-F., & Zagorec, M. (2015). Bacterial spoilers of food: Behavior, fitness and functional properties. *Food Microbiology, 45*(Part A), 45–53.

Ross, P., Mayer, R., & Benziman, M. (1991). Cellulose biosynthesis and function in bacteria. *Microbiological Reviews, 55*(1), 35–58.

Sarala Devi, G., Manorama, S., & Rao, V. J. (1995). High sensitivity and selectivity of an SnO2 sensor to H2S at around 100 °C. *Sensors and Actuators B, Chemical, 28*(1), 31–37.

Sarfraz, J., Ihalainen, P., Määttänen, A., Gulin, T., Koskela, J., Wilén, C. E., ... Peltonen, J. (2014). A printed H2S sensor with electro-optical response. *Sensors and Actuators B, Chemical, 191*, 821–827.

Schirmer, B. C., Heir, E., & Langsrud, S. (2009). Characterization of the bacterial spoilage flora in marinated pork products. *Journal of Applied Microbiology, 106*(6), 2106–2116.

Shah, N., Islam, M., Khattak, W., & Park, J. (2013). Overview of bacterial cellulose composites: A multipurpose advanced material. *Carbohydrate Polymers, 98*.

Shimizu, K., Imai, H., Hirashima, H., & Tsukuma, K. (1999). Low-temperature synthesis of anatase thin films on glass and organic substrates by direct deposition from aqueous solutions. *Thin Solid Films, 351*(1), 220–224.

Singhsa, P., Narain, R., & Manuspiya, H. (2018a). Bacterial cellulose nanocrystals (BCNC) preparation and characterization from three bacterial cellulose sources and development of functionalized BCNCs as nucleic acid delivery systems. *ACS Applied Nano Materials, 1*(1), 209–221.

Singhsa, P., Narain, R., & Manuspiya, H. (2018b). Physical structure variations of bacterial cellulose produced by different Komagataeibacter xylinus strains and carbon sources in static and agitated conditions. *Cellulose, 25*(3), 1571–1581.

Sofos, J. N. (1994). Microbial growth and its control in meat, poultry and fish. In A. M. Pearson, & T. R. Dutson (Eds.). *Quality attributes and their measurement in meat, poultry and Fish products* (pp. 359–403). Boston, MA: Springer US.

Solis, J. L., Saukko, S., Kish, L. B., Granqvist, C. G., & Lantto, V. (2001). Nanocrystalline tungsten oxide thick-films with high sensitivity to H2S at room temperature. *Sensors and Actuators B, Chemical, 77*(1), 316–321.

Susi, T., Pichler, T., & Ayala, P. (2015). X-ray photoelectron spectroscopy of graphitic carbon nanomaterials doped with heteroatoms. *Beilstein Journal of Nanotechnology, 6*, 177–192.

Szymańska-Chargot, M., Cybulska, J., & Zdunek, A. (2011). Sensing the structural differences in cellulose from apple and bacterial cell wall materials by Raman and FT-IR spectroscopy. *Sensors (Basel, Switzerland), 11*(6), 5543–5560.

Tang, J., Sisler, J., Grishkewich, N., & Tam, K. C. (2017). Functionalization of cellulose nanocrystals for advanced applications. *Journal of Colloid and Interface Science, 494*, 397–409.

Ummartyotin, S., & Manuspiya, H. (2015). A critical review on cellulose: From fundamental to an approach on sensor technology. *Renewable and Sustainable Energy Reviews, 41*(Supplement C), 402–412.

Vasconcelos, N. F., Feitosa, J. P. A., da Gama, F. M. P., Morais, J. P. S., Andrade, F. K., de Souza Filho, M. S. M., & Rosa, M. F. (2017). Bacterial cellulose nanocrystals produced under different hydrolysis conditions: Properties and morphological features. *Carbohydrate Polymers, 155*(Supplement C), 425–431.

Wada, M., Kondo, T., & Okano, T. (2003). Thermally induced crystal transformation from cellulose I to Iβ. *Polymer Journal, 35*, 155–159.

Wada, M., Okano, T., & Sugiyama, J. (2001). Allomorphs of native crystalline cellulose I evaluated by two equatoriald-spacings. *Journal of Wood Science, 47*(2), 124–128.

Wang, C., Chu, X., & Wu, M. (2006). Detection of H2S down to ppb levels at room temperature using sensors based on ZnO nanorods. *Sensors and Actuators B, Chemical, 113*(1), 320–323.

Winter, H. T., Cerclier, C., Delorme, N., Bizot, H., Quemener, B., & Cathala, B. (2010). Improved colloidal stability of bacterial cellulose nanocrystal suspensions for the elaboration of spin-coated cellulose-based model surfaces. *Biomacromolecules, 11*(11), 3144–3151.

Wu, J.-M., & Liu, R.-H. (2012). Thin stillage supplementation greatly enhances bacterial cellulose production by Gluconacetobacter xylinus. *Carbohydrate Polymers, 90*(1), 116–121.

Xu, J., Wang, X., & Shen, J. (2006). Hydrothermal synthesis of In2O3 for detecting H2S in air. *Sensors and Actuators B, Chemical, 115*(2), 642–646.

Yamamoto, H., Horii, F., & Hirai, A. (1996). In situ crystallization of bacterial cellulose II. Influences of different polymeric additives on the formation of celluloses Iα and Iβ at the early stage of incubation. *Cellulose, 3*(1), 229–242.

Yang, X., Zhu, Z., Liu, Q., Chen, X., & Ma, M. (2008). Effects of PVA, agar contents, and irradiation doses on properties of PVA/ws-chitosan/glycerol hydrogels made by γ-irradiation followed by freeze-thawing. *Radiation Physics and Chemistry, 77*(8), 954–960.

Zhang, G., Liao, Q., Zhang, Z., Liang, Q., Zhao, Y., Zheng, X., ... Zhang, Y. (2016). Novel piezoelectric paper-based flexible nanogenerators composed of BaTiO3 nanoparticles and bacterial cellulose. *Advanced Science, 3*(2) 1500257-n/a.